Hijacked Immune Cells Traverse Microenvironmental Barriers by Positioning and Pushing their Intracellular Parasite Cargo

Authors: Mauricio J.A. Ruiz-Fernandez[1], Jianfei Jiang[2,3], Armina Mortazavi[2,3], Bingzhi Wang[1], Artur Kuznetcov[1], Jack Merrin[4], Markus Meissner[5], Javier Periz[5]*, Benedikt Sabass[2,3]*, Jörg Renkawitz[1]*

Affiliations:

[1] Biomedical Center, Walter Brendel Center of Experimental Medicine, Institute of Cardiovascular Physiology and Pathophysiology, Klinikum der Universität, Ludwig-Maximilians-University Munich; Munich, Germany.

[2] Department for Veterinary Sciences, Institute for Infectious Diseases and Zoonoses, Ludwig-Maximilians-University Munich; Munich, Germany

[3] Faculty of Physics and Cetner for NanoScience, Ludwig-Maximilians-University Munich; Munich, Germany

[4] Institute of Science and Technology (IST) Austria; Klosterneuburg, Austria

[5] Experimental Parasitology, Department for Veterinary Sciences, Ludwig-Maximilians-University Munich; Munich, Germany

*Correspondence: Javier.Periz@para.vetmed.uni-muenchen.de, Benedikt.Sabass@micro.vetmed.uni-muenchen.de, and Joerg.Renkawitz@med.uni-muenchen.de.

Abstract:

Intracellular pathogens hijack the cytoskeletal networks of their host cells to facilitate their uptake, drive their intracellular motility, or prevent their degradation. While many underlying principles have been explored during host cell infections by intracellular bacteria like *Listeria*, *Chlamydia*, or *Shigella*, it remains less well understood how large eukaryotic intracellular parasites like *Toxoplasma gondii* exploit the host cytoskeleton. In particular, how *Toxoplasma* achieves its transport within highly motile immune cells remains largely unknown despite its large intracellular size. Here, we discover that *Toxoplasma gondii* hijacks host myosin forces for translocation through microenvironmental barriers along immune cell migration paths. Using highly defined micro-engineered migration paths and dendritic cells as a highly motile immune cell model, we reveal that large parasitic cargos acquire a surprising intracellular position frontward of the host nucleus and microtubule-organizing center. This frontward localization of parasitic cargos depends on microenvironmental confinement and host myosin activity. We identify that the parasite cargos cause high contractility within their motile host cells mediated by host myosin-II, thereby facilitating their squeezing and deformation to enable transversal through confining microenvironments. Our findings establish parasitic hijacking of myosin forces as a novel principle of how parasites exploit host cytoskeletal networks.

Keywords: *Toxoplasma gondii,* cytoskeletal forces, myosin, cell motility, organelle positioning, dendritic cells, microenvironmental pores.

Introduction

Mammalian cells are equipped with dynamic cytoskeletal structures that provide forces for cell shape dynamics, cell motility, organelle positioning, and intracellular transport[1–3]. Intracellular pathogens can hijack these forces generated by the host cell to (i) facilitate their uptake, (ii) drive their intracellular motility, or (iii) prevent their degradation[4]. For instance, various intracellular pathogens like the bacterium *Shigella flexneri* hijack and modulate the ability of host cells to engulf extracellular fluid by actin-dependent cellular protrusions in a process termed macropinocytosis, thereby facilitating their uptake and also release into the host cytoplasm[5–7]. The host actin cytoskeleton is further critical to provide a structural scaffold around vacuoles of the intracellular bacterium *Chlamydia* for vacuole stability [8]. Moreover, the intracellular bacteria *Listeria* and *Rickettsia* employ a comet-like movement within host cells to cross the plasma membrane of neighboring cells. The forces driving this fast intracellular movement originate from the host actin cytoskeleton, which is induced by the *Listeria* protein ActA that is anchored to the pathogen surface and stimulates the actin nucleation activity of the host actin nucleator Arp2/3[9], or by the *Rickettsia* protein Sca2 that has formin-like properties and thereby directly nucleates host actin in a linear manner[10]. Thus, hijacking of the host cell cytoskeleton is important for infection cycles of diverse bacterial pathogens.

However, whether and how the host cytoskeleton is exploited by large eukaryotic intracellular parasites is less well understood. The eukaryotic intracellular parasite *Leishmaniasis* generates a protective host actin coat around *Leishmania*-containing phagosomes[11] and also alters the host actin cytoskeleton of macrophages and dendritic cells to modulate their migratory ability[12]. The migratory capacity of dendritic cells is also well-known to be stimulated by the eukaryotic intracellular parasite *Toxoplasma gondii*, which induces a highly active migration mode of host dendritic cells [13,14]. Considering that *Toxoplasma gondii* (i) disseminates quickly from the host gut through the host organisms into lymph nodes and diverse tissues, and (ii) efficiently infects highly migratory host immune cells like dendritic cells, neutrophilic granulocytes, and T cells, *Toxoplasma gondii* appears to hijack the ability of host immune cells to move through tissues and to cross microenvironmental barriers[15,16]. However, such a model leads to a paradox, in which the large size of the parasitophorous vacuole that contains the replicating parasite[17] appears incompatible with the crossing of tissue microenvironments that are highly confining and contain pores that are substantially smaller than the host cell body and the parasitophorous vacuole[18].

While some studies observed efficient migration of immune cells loaded with *Toxoplasma* cargos within in vivo tissues and 3D collagen matrices, others observed limited crossing of microenvironmental barriers[19–21]. Thus, it remains unknown whether and how *Toxoplasma* achieves its intracellular transport as a bulky cargo in immune cells. Also more generally, how do large intracellular parasites exploit the mechanics and forces of host cells to efficiently cross microenvironmental barriers efficiently?

To address this knowledge gap, we here generated micro-engineered microenvironments that allowed us to investigate the crossing of *Toxoplasma* cargos within motile immune cells through space-limiting microenvironments in a quantifiable throughput manner. Thereby, we discover that *Toxoplasma* hijacks myosin-driven forces of the host cell for dynamic intracellular repositioning and for crossing microenvironmental barriers,

86 providing a new principle of how intracellular pathogens hijack the cellular forces and
87 mechanics of the host.
88

89 Results

90 Unfolding and deformation of the parasitophorous vacuole cargo during immune cell 91 crossing of microenvironmental barriers

92 To address the paradox of how motile immune cells transport large intracellular parasitic cargos
93 efficiently, we employed mouse dendritic cells (DCs) as a well-established highly migratory
94 cellular model and *Toxoplasma gondii* as a well-established eukaryotic intracellular parasite
95 model. Upon timed infection, we loaded the parasite-bearing DCs into microchannels with a
96 defined width of 8 micrometers and height of 5 micrometers, providing a straight tunnel-like
97 track for motility. Using fluorescently tagged *Toxoplasma* parasites and simultaneous imaging
98 of hundreds of microchannels allowed us to precisely quantify the migratory velocity for the
99 first time depending on the replication stage of the parasite. These measurements showed that
100 dendritic cells loaded with 1-, 2-, and 4-stage parasites have high migratory velocities of around
101 10 micrometers per minute, comparable to the velocity of non-infected bystander DCs (Fig. 1a,
102 b). Yet, when the parasites further replicated to 8-, 16-, and 32-stages, in which the
103 parasitophorous vacuole (PV) that contains the individual parasites is even larger than the host
104 nucleus (Fig. 1c), decreased the host cell velocity (Fig. 1b). Nevertheless, even extremely large
105 16- and 32-stage PVs that entirely filled the width of the microchannels and large parts of the
106 host cytoplasm, still migrated with substantial speeds of 2-6 micrometers per minute (Fig. 1a-
107 c). These findings showed that microenvironmental confinement slows the migration of
108 immune cells loaded with very large parasitic cargos, but also suggested that even extremely
109 large parasitic cargo transport is rather efficient.
110 To identify the limits of parasitic cargo transport within motile DCs, we introduced a
111 defined pore of 4-micrometers widths into the migratory track. While larger parasitic cargos
112 took longer to squeeze through the pore, they still passed surprisingly efficiently (Fig. 1d). To
113 provide a smaller pore that is even smaller than an individual parasite, we next introduced pores
114 with widths of only 2 micrometers, and still observed high rates of cellular passage, even when
115 loaded with large parasitic cargos (Fig. 1e).
116 To understand how this large, bulky, and stiff parasitic cargo is translocated through
117 narrow microenvironmental pores, we next performed fast time-lapse and high-resolution
118 imaging of labeled parasites. These measurements revealed a sequential passage of parasites
119 within a PV through the pores, followed by a rapid PV reorganization behind the pore (Fig. 1f).
120 Squeezing-like deformations of individual parasites accompanied this unfolding-like behavior
121 of the parasitic PV while they translocated through the pore, substantially deforming the
122 ellipsoid shape of *Toxoplasma gondii* (Fig. 1g). Notably, the individual parasites frequently
123 resided for some time during their invasion into the pore, which was followed by a quick
124 translocation through the pore once the entire parasite was deformed (Fig. 1i), further
125 underscoring the stiffness of the parasite. Together, these findings demonstrate that
126 intracellular *Toxoplasma* parasites are a large, bulky, and stiff cargo within motile dendritic
127 cells, thereby representing a bottleneck during migration through microenvironmental pores.
128 However, the translocation of the parasite through narrow pores by PV unfolding and parasite

squeezing also suggests that the parasite employs mechanisms that enable its efficient transport as cargo while immune cells quickly migrate through confining microenvironments.

Dynamic intracellular repositioning of large parasitic cargos towards the cell front of motile immune cells.

To identify the mechanisms of how the parasite organizes its efficient transport as cargo, we imaged the intracellular position of the parasite in relation to the host nucleus and the microtubule-organising center (MTOC), both serving as indicators for the underlying cell polarity and thus cytoskeletal forces. To our surprise, we observed that parasitic cargos are frequently positioned frontward of the host DC nucleus during the migration through maze-like microenvironments (Fig. 2a). Given that DCs belong to the class of migrating cells that employ an amoeboid migration mode that is characterized by low-adhesiveness to the substrate and frontward positioning of the nucleus towards the cellular protrusion[3,22], this even more frontward positioning of the parasitic cargo in relation to the host nucleus was highly unexpected. Notably, quantification of parasite positioning in relation to the parasite stage revealed that large parasitic 8- and 16-stage cargos particularly frequently positioned in front of the host nucleus (Fig. 2a). To confirm this finding, we loaded parasite-infected DCs in 8 micrometers wide linear microchannels, allowing us to precisely map the intracellular positioning of the parasite independent of directional changes of the host cell (Fig. 2b). Quantification confirmed an increasing frontward positioning of the PV cargo with increasing PV-stage and -size, in which very small 1-stage PV cargos are mostly positioned in the back of the host nucleus, whereas very large 32-stage PV cargos are mostly positioned in the front (Fig. 2c). In agreement with this finding, we frequently observe repositioning of large parasitic cargos from the rear to the front during our imaging intervals but rarely vice versa (Fig. 2d, e), demonstrating that large parasitic cargos actively acquire their frontward intracellular localisation.

To map this surprising intracellular position of the parasitic cargo more precisely, we infected EB3-mcherry expressing DCs, serving as a microtubule-plus end and microtubule-organising center (MTOC) marker with the motile host cells (Fig. 2f). This revealed that large parasitic cargos are mostly positioned frontward of the MTOC (Fig. 2g), which typically localizes approximately to the center of cells. Moreover, in most cases the large parasitic cargo is even positioned together with the nucleus in front of the MTOC (Fig. 2h), showing that both can acquire an amoeboid-like frontward positioning. These findings together uncover that large parasitic cargos are positioned towards the cell front despite their large and bulky nature.

Interestingly, when we loaded passive beads with a diameter of 6 micrometers into parasite-infected DCs, we observed a rather random intracellular localization of the passive beads, being mostly positioned behind the parasitic cargo (Fig. 2i), suggesting that the parasite may actively drive its positioning with increasing PV-stage. Notably, 4- and 8-stage PVs represent the transition point of when the parasitic cargo begins to be preferentially positioned towards the cell front, correlating with a parasitic size that is large enough to be in the close vicinity of the microenvironmental substrate in 8 micrometers wide microchannels. Thus, we speculated that the frontward positioning of large parasite cargo may be based on a mechanism that senses the microenvironmental confinement of the parasitic cargo. To test this model, we loaded parasite-infected DCs into more-wide channels with widths of 10- or 16 micrometers.

173 Quantification indeed revealed that these wider-spaced microenvironments required larger
174 parasitic cargos to observe the frontward positioning of the parasitic cargo in comparison to
175 the 8 micrometers-wide microchannels (Fig, 2j, k). Together, these findings reveal that large
176 parasitic cargos are dynamically positioned towards the cell front, particularly in confining
177 microenvironments. Given that the parasitic cargo is not simply dragged at the very cell rear,
178 these data identify the existence of forces that move and position the parasitic cargo.
179
180 **Host cell myosin drives the dynamic repositioning of large parasitic cargos.**
181 To identify the forces that move the bulky parasitic cargo intracellularly, we targeted key
182 cytoskeletal force generators within the host cell. Host cells position specific sets of their
183 organelles by forces derived from the microtubule cytoskeleton and its motors[3], including the
184 pulling of the large and bulky nucleus in mesenchymal migrating cells[23]. However, the above-
185 described positioning of *Toxoplasma gondii* parasites within DCs far frontward of the
186 microtubule organizing center rather argued against a mechanism that employs microtubule
187 forces to pull the bulky parasitic cargo. Indeed, when we analyzed the positioning of the
188 parasite cargo upon microtubule depolymerization, we did not observe any impaired frontward
189 positioning of large parasitic cargo (Fig. 3a). Rather in contrast, cells with a depolymerized
190 microtubule cytoskeleton may tend to position their large parasitic cargo even more likely to
191 the front of the cell (Fig. 3a), largely excluding microtubules as a major driving force for the
192 intracellular position of *Toxoplasma gondii* in motile DCs.
193 Given that microtubule-depolymerisation is well-known to induce cellular contractility
194 via myosin, the finding that microtubule-depolymerisation may cause a more likely frontward
195 positioning of large cargos suggested that forces originating from myosin may drive the
196 intracellular movement and positioning of the parasite. In line with this notion, we often
197 observed a smooth roundish cell front in *Toxoplasma gondii*-infected DCs (Fig. 3b) and even
198 occasionally cells with a blebbing cell front during migration, both indicators of a high degree
199 of intracellular contractility. This finding was surprising, as DCs have not yet been described
200 to employ a blebbing-like migration mode, which is used by some cell types for forward
201 movement[24,25]. As DCs typically have cell fronts composed of highly dynamic veil-like
202 protrusions, this finding indicated a shift in the balance of cellular progressiveness and
203 contractility[26] upon parasite infection. Notably, when we quantified the frequency of this
204 smooth cell front phenotype in relation to the replication stage of the parasite, we observed that
205 large parasitic cargos almost always caused the appearance smooth roundish DC cell front (Fig.
206 3b). This phenotype was appeared even with smaller parasitic cargos upon host cell
207 microtubule depolymerization (Fig. 3b), again suggesting an increased myosin-based cell
208 contractility in *Toxoplasma gondii*-infected DCs.
209 To directly test this hypothesis, we first imaged the localization of host myosin by
210 infecting Myh9-GFP expressing DCs to visualize host myosin-IIA (Fig. 3c). Live cell imaging
211 revealed a strong enrichment of myosin-IIA in the rear of the cell behind the parasitic cargo
212 (Fig. 3c). While uninfected DCs also often show a rearward accumulation, the distribution
213 pattern is often more distributed intracellularly. However, with the increasing parasite
214 replication stage, we observed an increasing frequency of a clearly defined rearward
215 enrichment of host myosin-IIA (Fig. 3d), showing that large parasitic cargos cause a shift in
216 the distribution of myosin-IIA. This strong rearward accumulation of myosin suggested a

model in which myosin-based contractility at the cell rear cause a contractile force that pushes the parasitic cargo. To directly test this model, we employed the myosin-inhibitor para-nitro blebbistatin and measured the positioning of the parasitic cargo during DC migration. While in control cells the frontward position of the parasite cargo increased with increasing parasite stages, inhibited cells showed an overall mostly random localization pattern (Fig. 3e). This finding was substantiated when we analyzed the frequency of how often the PV cargo moves to the front in our imaging periods, revealing that myosin-inhibition strongly impaired the ability of parasitic cargos to move toward the cell front of infected-DCs (Fig. 3f). Together, these data show that *Toxoplasma gondii* parasites hijack forces from host myosin contractility. Considering that this particularly occurs with large parasitic cargos shows that parasites are able to adapt their hijacking strategy to the size of the parasite.

Intracellular parasitic repositioning and host cell contractility facilitate crossing of microenvironmental barriers.

To address whether *Toxoplasma gondii* does not only hijack host myosin contractility for its own intracellular movement but also to overcome microenvironmental barriers that motile immune cells face on their trafficking paths, we quantified the velocity of parasite-loaded motile DCs upon myosin inhibition. This showed that uninfected bystander cells achieve the same velocities in the presence of the myosin inhibitor para-nitro blebbistatin as control cells (Fig. 4a). Similarly, also parasite-infected cells with small 1-stage PVs showed non-impaired migration velocities (Fig. 4a). However, with increasing PV stages and thus sizes of the parasite cargo, myosin inhibition caused impaired migration through 8 micrometers-wide microchannels (Fig. 4a), suggesting that migration of parasite cargos with sizes being confined in the microenvironment may require host myosin activity.

To directly mimic confined microenvironments, we next investigated how often parasite-infected DCs passed 2 micrometers pores. While almost all control cells efficiently translocated through these tiny pores (as shown in Figure 1), myosin inhibition caused a strong impairment of larger PV to cross these pores (Fig. 4b). While small 1- and 2-stage parasites still sometimes migrated through the pores, large 4-, 8-, and 16-stages almost always got entirely stuck at the 2 micrometer-sized pores (Fig. 4b). Notably, when we imaged the behaviour of parasite-loaded DCs that get stuck at the pore entrance when myosin function is impaired, we noticed egress of the parasite out of the host cell (Fig. 4c). Quantification in relation to the PV cargo revealed that egress was rare in control cells but particularly frequently occurring with large parasitic cargos upon impairement of myosin activity (Fig. 4c). Together, these data discover that *Toxoplasma gondii* hijacks the myosin contractility of the host cell to achieve its transport during the highly dynamic migration of dendritic cells through complex and confining microenvironments. These data further discover that this hijacking mode adapts to the size of the parasite cargo, providing forces when they are most needed, namely to move and squeeze particularly large intracellular parasitic cargos.

Discussion

Parasites can facilitate their dissemination within the host organism by intracellular transport in highly motile immune cells. Whereas the dissemination of the eukaryotic parasite *Toxoplasma gondii* by long-range transport between different tissues within a single immune cell is highly debated[15] and appears unlikely, facilitated dissemination by a 'hop-on hop-off'-like mechanism with multiple cycles of infection and egress using different individual motile immune cells is strongly supported by several pieces of evidence: *Toxoplasma gondii* (i) infects efficiently and early immune cells in the gut of their host upon uptake by food, (ii) arrives already after a few days in the lymph nodes, which represent the homing destination of many highly motile immune cells, and (iii) even induces a high motile mode of immune cells once they are infected[15,27]. However, considering the bulky nature of the parasitophorous vacuole - in which the parasite replicates - within its host cells, it remained entirely unknown how fast immune cell migration through the complex and confining microenvironment of tissues is compatible with such a bulky cargo. Here, we identify that the parasitic cargo is indeed larger and likely even stiffer than the host nucleus. This finding was surprising, as the host nucleus is already well-known to be a bottleneck for cell motility through environmental pores[2,28], given its large size and high stiffness in comparison to other cellular organelles[29]. Employing hundreds of microchannels with defined microenvironmental topography in parallel, allowed us to here discover how the parasite overcomes this paradox. We identify that the parasite causes a rearward accumulation of myosin, fostering a presumably frontward-driven cellular contractility from the cell rear to drive the movement of the parasite within the host cytoplasm and through microenvironmental confinement. If this myosin II-driven contractility is impaired, the parasitic cargo and thus the entire immune cell gets stuck at narrow pores, preventing parasite dissemination and causing local egress. Together, these findings identify the principle of pathogen hijacking of host myosin contractility for efficient parasite cargo transport. Further, our findings identify that *Toxoplasma gondii* modulates the forces of the host cytoskeleton with its own size to an increasing extent, thereby discovering that parasites can adapt their hijacking of the host cytoskeleton to the nature of the parasitic cargo.

290 **References**

291

292 1. Fletcher, D.A., and Mullins, R.D. (2010). Cell mechanics and the cytoskeleton. Nature
293 *463*, 485–492. 10.1038/nature08908.

294 2. Yamada, K.M., and Sixt, M. (2019). Mechanisms of 3D cell migration. Nature Reviews
295 Molecular Cell Biology *20*, 738–752. 10.1038/s41580-019-0172-9.

296 3. Kroll, J., and Renkawitz, J. (2024). Principles of organelle positioning in motile and non-
297 motile cells. EMBO Rep., 1–16. 10.1038/s44319-024-00135-4.

298 4. Kühn, S., and Enninga, J. (2020). The actin comet guides the way: How Listeria actin
299 subversion has impacted cell biology, infection biology and structural biology. Cell.
300 Microbiol. *22*, e13190. 10.1111/cmi.13190.

301 5. Weiner, A., Mellouk, N., Lopez-Montero, N., Chang, Y.-Y., Souque, C., Schmitt, C., and
302 Enninga, J. (2016). Macropinosomes are Key Players in Early Shigella Invasion and
303 Vacuolar Escape in Epithelial Cells. PLoS Pathog. *12*, e1005602.
304 10.1371/journal.ppat.1005602.

305 6. Chang, Y., Enninga, J., and Stévenin, V. (2021). New methods to decrypt emerging
306 macropinosome functions during the host–pathogen crosstalk. Cell. Microbiol. *23*, e13342.
307 10.1111/cmi.13342.

308 7. Mercer, J., and Helenius, A. (2009). Virus entry by macropinocytosis. Nature cell biology
309 *11*, 510–520. 10.1038/ncb0509-510.

310 8. Kumar, Y., and Valdivia, R.H. (2008). Actin and Intermediate Filaments Stabilize the
311 Chlamydia trachomatis Vacuole by Forming Dynamic Structural Scaffolds. Cell Host
312 Microbe *4*, 159–169. 10.1016/j.chom.2008.05.018.

313 9. Welch, M.D., Rosenblatt, J., Skoble, J., Portnoy, D.A., and Mitchison, T.J. (1998).
314 Interaction of Human Arp2/3 Complex and the Listeria monocytogenes ActA Protein in
315 Actin Filament Nucleation. Science *281*, 105–108. 10.1126/science.281.5373.105.

316 10. Haglund, C.M., Choe, J.E., Skau, C.T., Kovar, D.R., and Welch, M.D. (2010). Rickettsia
317 Sca2 is a bacterial formin-like mediator of actin-based motility. Nat. Cell Biol. *12*, 1057–
318 1063. 10.1038/ncb2109.

319 11. Lodge, R., and Descoteaux, A. (2005). Leishmania donovani promastigotes induce
320 periphagosomal F-actin accumulation through retention of the GTPase Cdc42. Cell.
321 Microbiol. *7*, 1647–1658. 10.1111/j.1462-5822.2005.00582.x.

322 12. Luz, Y., Rebouças, A., Bernardes, C.P.O.S., Rossi, E.A., Machado, T.S., Souza, B.S.F.,
323 Brodskyn, C.I., Veras, P.S.T., Santos, W.L.C. dos, and Menezes, J.P.B. de (2023).
324 Leishmania infection alters macrophage and dendritic cell migration in a three-dimensional
325 environment. Front. Cell Dev. Biol. *11*, 1206049. 10.3389/fcell.2023.1206049.

326 13. Lambert, H., Hitziger, N., Dellacasa, I., Svensson, M., and Barragan, A. (2006). Induction
327 of dendritic cell migration upon Toxoplasma gondii infection potentiates parasite
328 dissemination. Cellular microbiology *8*, 1611–1623. 10.1111/j.1462-5822.2006.00735.x.

329 14. Weidner, J.M., Kanatani, S., Castañeda, M.A.H., Fuks, J.M., Rethi, B., Wallin, R.P.A.,
330 and Barragan, A. (2013). Rapid cytoskeleton remodelling in dendritic cells following
331 invasion by Toxoplasma gondii coincides with the onset of a hypermigratory phenotype.
332 Cellular microbiology *15*, 1735–1752. 10.1111/cmi.12145.

333 15. Drewry, L.L., and Sibley, L.D. (2019). The hitchhiker's guide to parasite dissemination.
334 Cell Microbiol *21*, e13070. 10.1111/cmi.13070.

335 16. Ólafsson, E.B., and Barragan, A. (2020). The unicellular eukaryotic parasite Toxoplasma
336 gondii hijacks the migration machinery of mononuclear phagocytes to promote its
337 dissemination. Biol Cell *112*, 239–250. 10.1111/boc.202000005.

338 17. Clough, B., and Frickel, E.-M. (2017). The Toxoplasma Parasitophorous Vacuole: An
339 Evolving Host–Parasite Frontier. Trends Parasitol *33*, 473–488. 10.1016/j.pt.2017.02.007.

340 18. Kameritsch, P., and Renkawitz, J. (2020). Principles of Leukocyte Migration Strategies.
341 Trends Cell Biol *30*, 818–832. 10.1016/j.tcb.2020.06.007.

342 19. Bhandage, A.K., Olivera, G.C., Kanatani, S., Thompson, E., Loré, K., Varas-Godoy, M.,
343 and Barragan, A. (2020). A motogenic GABAergic system of mononuclear phagocytes
344 facilitates dissemination of coccidian parasites. Elife *9*, e60528. 10.7554/elife.60528.

345 20. Drewry, L.L., Jones, N.G., Wang, Q., Onken, M.D., Miller, M.J., and Sibley, L.D. (2019).
346 The secreted kinase ROP17 promotes Toxoplasma gondii dissemination by hijacking
347 monocyte tissue migration. Nat Microbiol *4*, 1951–1963. 10.1038/s41564-019-0504-8.

348 21. Sangaré, L.O., Ólafsson, E.B., Wang, Y., Yang, N., Julien, L., Camejo, A., Pesavento, P.,
349 Sidik, S.M., Lourido, S., Barragan, A., et al. (2019). In Vivo CRISPR Screen Identifies
350 TgWIP as a Toxoplasma Modulator of Dendritic Cell Migration. Cell Host Microbe *26*, 478-
351 492.e8. 10.1016/j.chom.2019.09.008.

352 22. Renkawitz, J., Kopf, A., Stopp, J., Vries, I. de, Driscoll, M.K., Merrin, J., Hauschild, R.,
353 Welf, E.S., Danuser, G., Fiolka, R., et al. (2019). Nuclear positioning facilitates amoeboid
354 migration along the path of least resistance. Nature *568*, 546–550. 10.1038/s41586-019-1087-
355 5.

356 23. Calero-Cuenca, F.J., Janota, C.S., and Gomes, E.R. (2018). Dealing with the nucleus
357 during cell migration. Current Opinion in Cell Biology *50*, 35–41.
358 10.1016/j.ceb.2018.01.014.

359 24. García-Arcos, J.M., Jha, A., Waterman, C.M., and Piel, M. (2024). Blebology: principles
360 of bleb-based migration. Trends Cell Biol. 10.1016/j.tcb.2024.02.009.

361 25. Paluch, E.K., and Raz, E. (2013). The role and regulation of blebs in cell migration.
362 Current Opinion in Cell Biology *25*, 582–590. 10.1016/j.ceb.2013.05.005.

363 26. Lämmermann, T., and Sixt, M. (2009). Mechanical modes of “amoeboid” cell migration.
364 Current Opinion in Cell Biology *21*, 636–644. 10.1016/j.ceb.2009.05.003.

365 27. Matta, S.K., Rinkenberger, N., Dunay, I.R., and Sibley, L.D. (2021). Toxoplasma gondii
366 infection and its implications within the central nervous system. Nat Rev Microbiol, 1–14.
367 10.1038/s41579-021-00518-7.

368 28. Wolf, K., Lindert, M. te, Krause, M., Alexander, S., Riet, J. te, Willis, A.L., Hoffman,
369 R.M., Figdor, C.G., Weiss, S.J., and Friedl, P. (2013). Physical limits of cell migration:
370 Control by ECM space and nuclear deformation and tuning by proteolysis and traction force.
371 J Cell Biol *201*, 1069–1084. 10.1083/jcb.201210152.

372 29. Kalukula, Y., Stephens, A.D., Lammerding, J., and Gabriele, S. (2022). Mechanics and
373 functional consequences of nuclear deformations. Nat Rev Mol Cell Bio, 1–20.
374 10.1038/s41580-022-00480-z.

375 30. Redecke, V., Wu, R., Zhou, J., Finkelstein, D., Chaturvedi, V., High, A.A., and Häcker,
376 H. (2013). Hematopoietic progenitor cell lines with myeloid and lymphoid potential. Nature
377 methods *10*, 795–803. 10.1038/nmeth.2510.

378 31. Li, W., Grech, J., Stortz, J.F., Gow, M., Periz, J., Meissner, M., and Jimenez-Ruiz, E.
379 (2022). A splitCas9 phenotypic screen in Toxoplasma gondii identifies proteins involved in
380 host cell egress and invasion. Nat. Microbiol. *7*, 882–895. 10.1038/s41564-022-01114-y.

381 32. Rosario, M.D., Periz, J., Pavlou, G., Lyth, O., Latorre-Barragan, F., Das, S., Pall, G.S.,
382 Stortz, J.F., Lemgruber, L., Whitelaw, J.A., et al. (2019). Apicomplexan F-actin is required
383 for efficient nuclear entry during host cell invasion. EMBO Rep. *20*, e48896.
384 10.15252/embr.201948896.

385 33. Kroll, J., Ruiz-Fernandez, M.J.A., Braun, M.B., Merrin, J., and Renkawitz, J. (2022).
386 Quantifying the Probing and Selection of Microenvironmental Pores by Motile Immune
387 Cells. Curr Protoc *2*, e407. 10.1002/cpz1.407.

388 34. Schindelin, J., Arganda-Carreras, I., Frise, E., Kaynig, V., Longair, M., Pietzsch, T.,
389 Preibisch, S., Rueden, C., Saalfeld, S., Schmid, B., et al. (2012). Fiji: an open-source platform
390 for biological-image analysis. Nature methods *9*, 676–682. 10.1038/nmeth.2019.

391
392
393

394 # Figures and figure legends

395

396

397

Figure 1. Unfolding and deformation of the parasitophorous vacuole cargo during immune cell crossing of microenvironmental barriers.

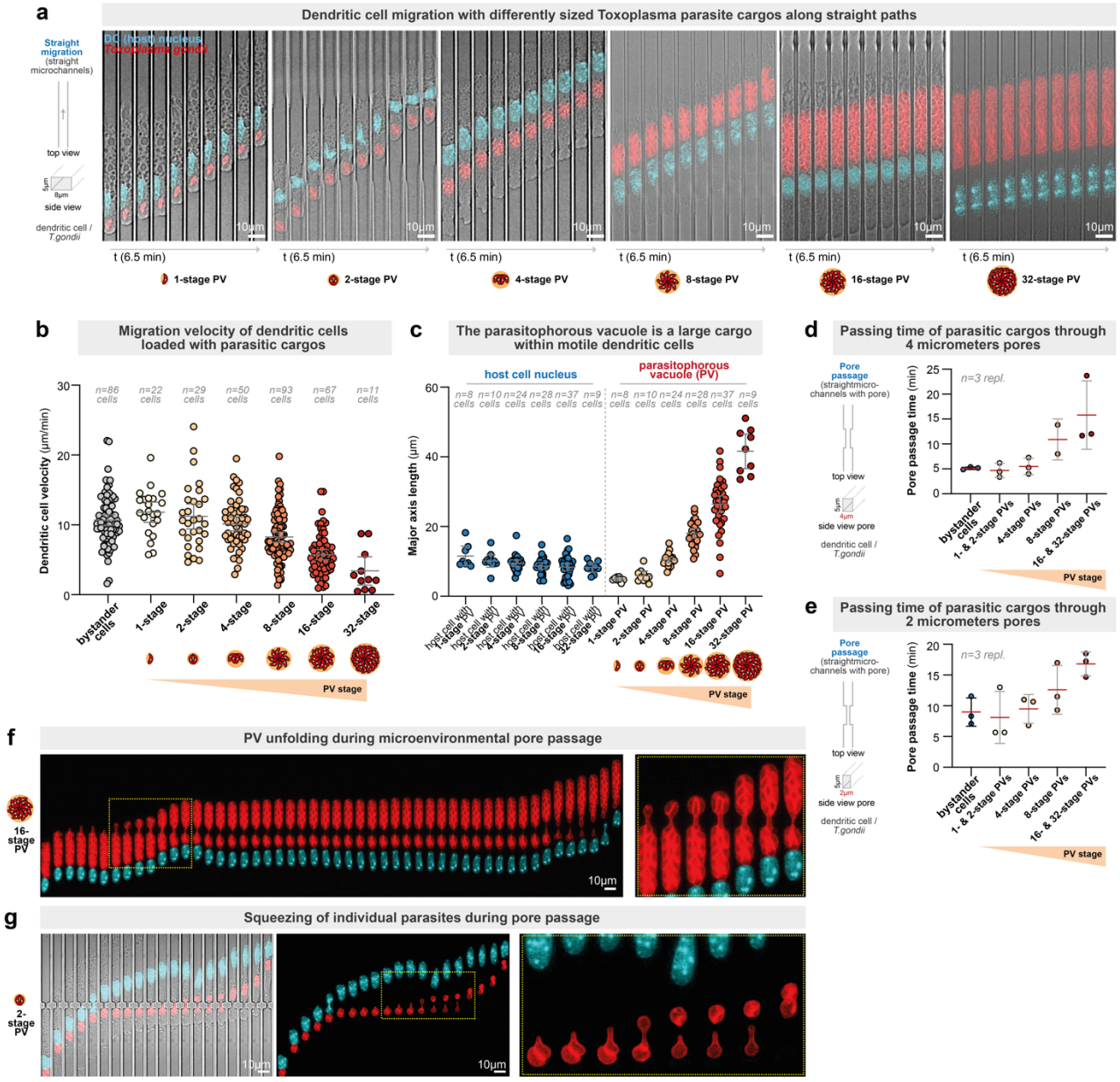

398

399

Figure 1. Unfolding and deformation of the parasitophorous vacuole cargo during immune cell crossing of microenvironmental barriers. (A) Representative *Toxoplasma gondii*-infected dendritic cells (DCs) migrating in linear microchannels. Note the different replication stages (1- to 32-stage) of the parasite within the motile host cell. *Toxoplasma gondii* is shown in red, the host DC nucleus in cyan (Hoechst), and the imaging medium contained DMSO. **(B)** Quantification of a) of the DC velocity in relation to the replication stage of the parasite cargo. N= 86 cells (non-infected bystander DCs), 22 cells (1-stage PV), 29 cells (2-stage PV), 50 cells (4-stage PV), 93 cells (8-stage PV), 67 cells (16-stage PV), and 11 cells (32-stage PV) from 3 independent biological replicates. Data are mean±95% CI. **(C)** Length of the parasitophorous vacuole in comparison to the host cell nucleus during DC migration along linear microchannels as shown in a). N= 8 cells (1-stage PV), 10 cells (2-stage PV), 24 cells (4-stage PV), 28 cells (8-stage PV), 37 cells (16-stage PV), and 9 cells (32-stage PV) from 3 independent biological replicates. Data are mean±95% CI. **(D)** Passing times of parasitic cargos of different sizes during DC migration through 4 micrometers-sized pores. Data are mean±SD. **(E)** Passing times of parasitic cargos of different sizes during DC migration through 2 micrometers-sized pores. Data are mean±SD. **(F)** Representative 16-stage example of unfolding of the parasitophorous vacuole (PV) during passage through a 2 micrometers-sized pore. The yellow dashed square is shown as a zoom. **(G)** Representative example of squeezing of individual parasites within a 2-stage parasitophorous vacuole (PV) during passage through a 2 micrometers-sized pore. The yellow dashed square is shown as a zoom.

Figure 2. Dynamic intracellular repositioning of large parasitic cargos towards the cell front of motile immune cells.

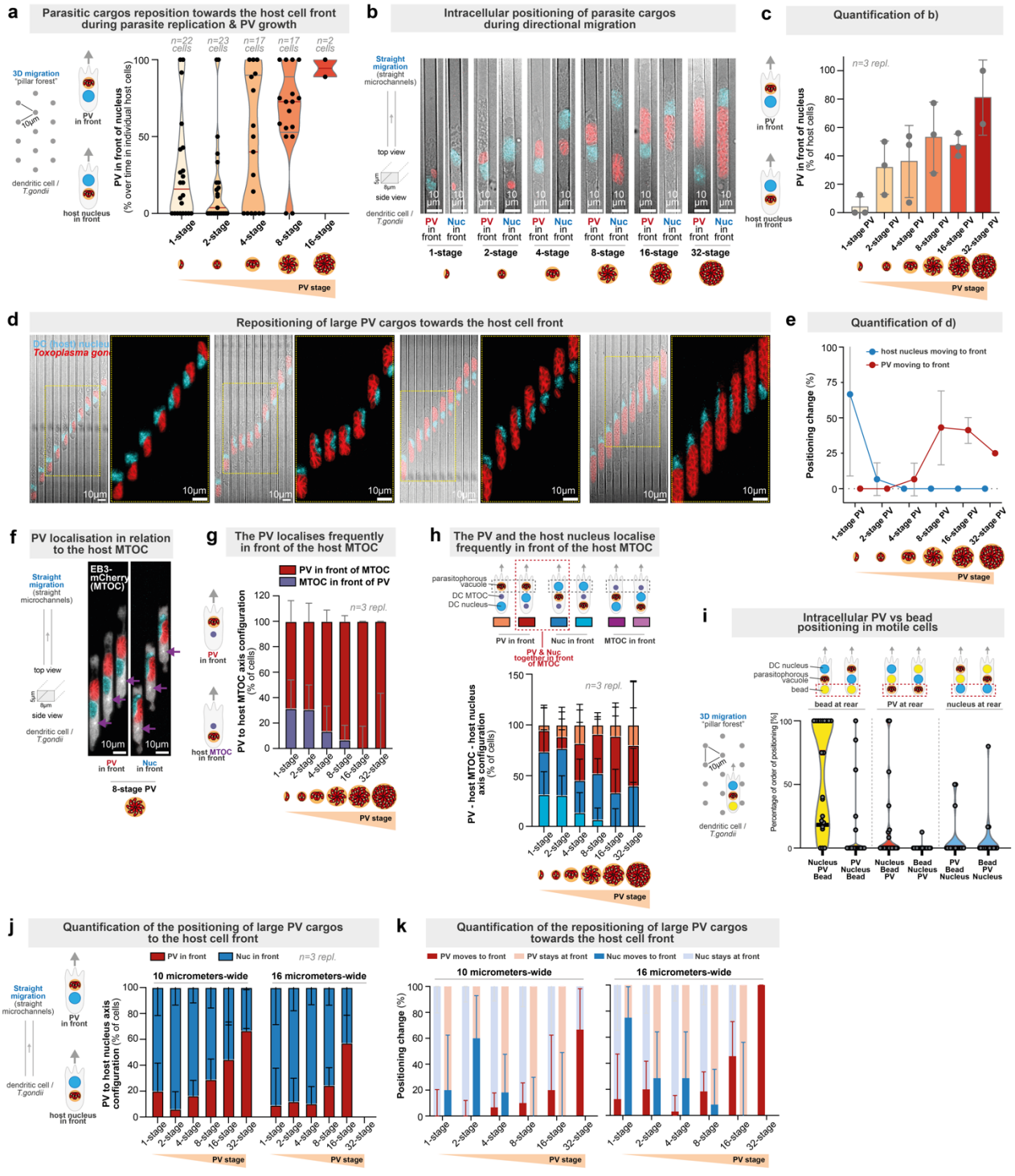

Figure 2. Dynamic intracellular repositioning of large parasitic cargos towards the cell front of motile immune cells. (A) Positioning of the parasitophorous vacuole (PV) in relation to the host cell nucleus during migrating of toxoplasma-infected dendritic cells (DCs) through a maze of pillars (10 micrometer spacing between pillars). N= 22 cells (1-stage PV), 23 cells (2-stage PV), 17 cells (4-stage PV), 17 cells (8-stage PV), 2 cells (16-stage PV) from 3 independent biological replicates. Data are mean±95% CI. **(B)** Representative examples of PV positioning in relation to the host cell nucleus during DC migration in a straight 8 micrometer-wide microchannel. *Toxoplasma gondii* in red, host cell nucleus in cyan. **(C)** Quantification of the positioning of the parasite cargo in relation to the host nucleus as shown in b) in the presence of DMSO. N=3 individual biological replicates. **(D)** Representative examples of the repositioning of large PV cargos towards the host cell front into the front of the host nucleus. **(E)** Quantification of d). **(F)** Representative example of EB3-mcherry expressing dendritic cells (white; label for the MTOC) infected with *Toxoplasma gondii* shown in red. The host nucleus is shown in cyan **(G)** Quantification of the PV to MTOC positioning as shown in f). N=3 individual biological replicates. **(H)** Quantification of the PV to MTOC to nucleus positioning as shown in f). N=3 individual biological replicates. **(I)** Quantification of the PV to nucleus axis configuration in relation to latex beads. N=3 individual biological replicates. **(J)** Quantification of the PV to nucleus axis configuration during migration in wider 10 and 16 micrometers channels. N=3 individual biological replicates. **(K)** As in J, but showing the repositioning of PV cargos towards the host cell front into the front of the host nucleus. N=3 individual biological replicates.

455
456

Figure 3. Host cell myosin drives the dynamic repositioning of large parasitic cargos.

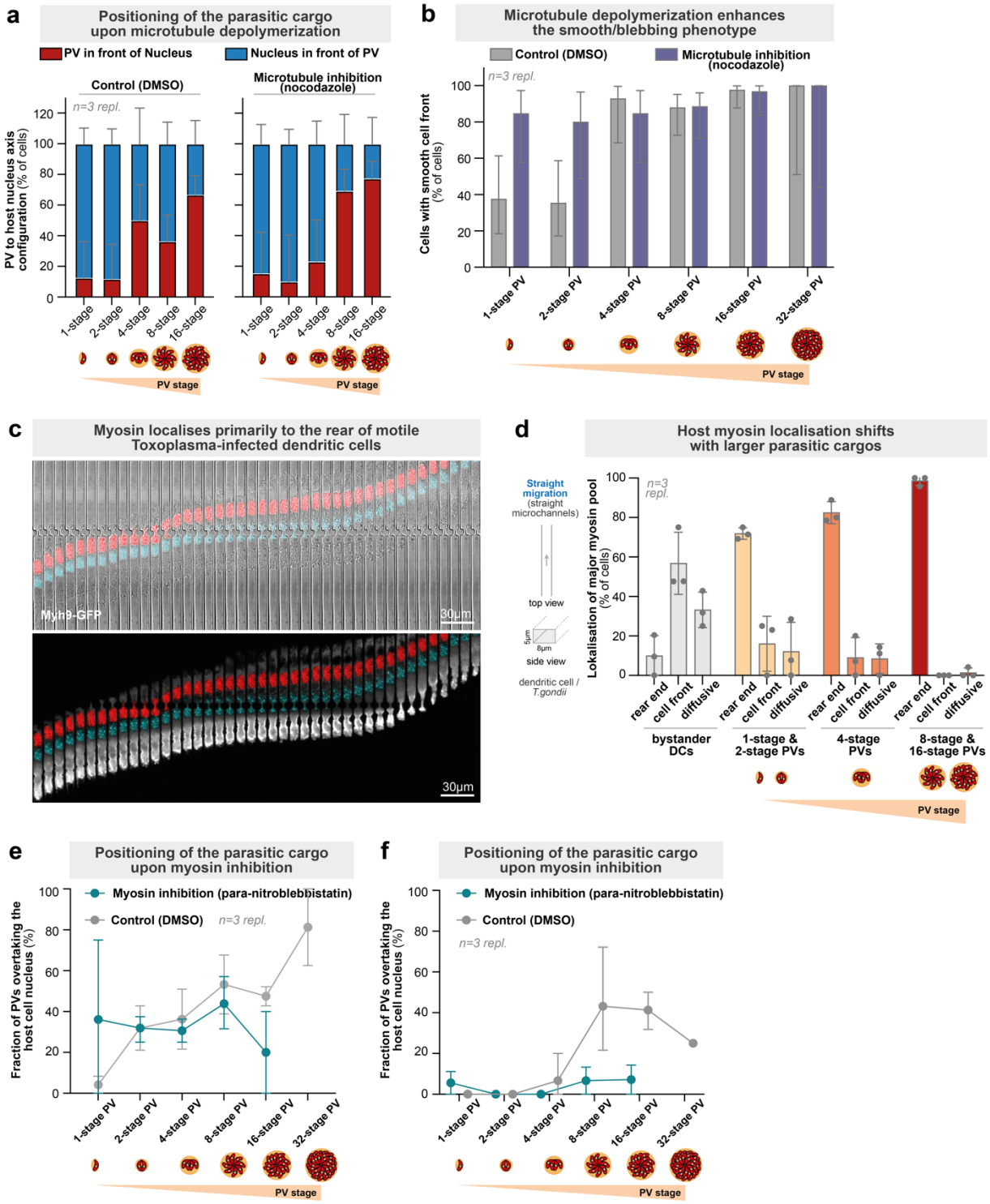

457
458
459

460 **Figure 3. Host cell myosin drives dynamic repositioning of large parasitic cargos. (A)**
461 Quantification of the positioning of the parasitic cargo in relation to the host nucleus in the
462 presence of the microtubule inhibitor nocodazole or DMSO controls. N=3 individual biological
463 replicates. **(B)** Quantification of the smooth cell front phenotype in the presence of the
464 microtubule inhibitor nocodazole or DMSO controls. N=3 individual biological replicates. **(C)**
465 Representative examples of Myh9-GFP expressing DCs (myosin-IIA; shown in white) infected
466 with *Toxoplasma gondii* (shown in red). The host nucleus is shown in cyan. **(D)** Quantification
467 of the major localization of the Myh9-GFP signal in relation to the replication stage. N=3
468 individual biological replicates. **(E)** Positioning of the parasitic cargo in presence of the myosin
469 II inhibitor para-nitro-blebbistatin or DMSO controls. Note that the control cells are the same
470 as plotted in Fig 2c. N=3 individual biological replicates. **(F)** Repositioning of the parasitic
471 cargo toward the cell front into the front of the host nucleus in presence of the myosin II
472 inhibitor para-nitro-blebbistatin or DMSO controls. Note that the control cells are the same as
473 plotted in Fig 2e. N=3 individual biological replicates.
474
475

Figure 4. Intracellular parasitic repositioning and host cell contractility faciliate crossing of microenvironmental barriers.

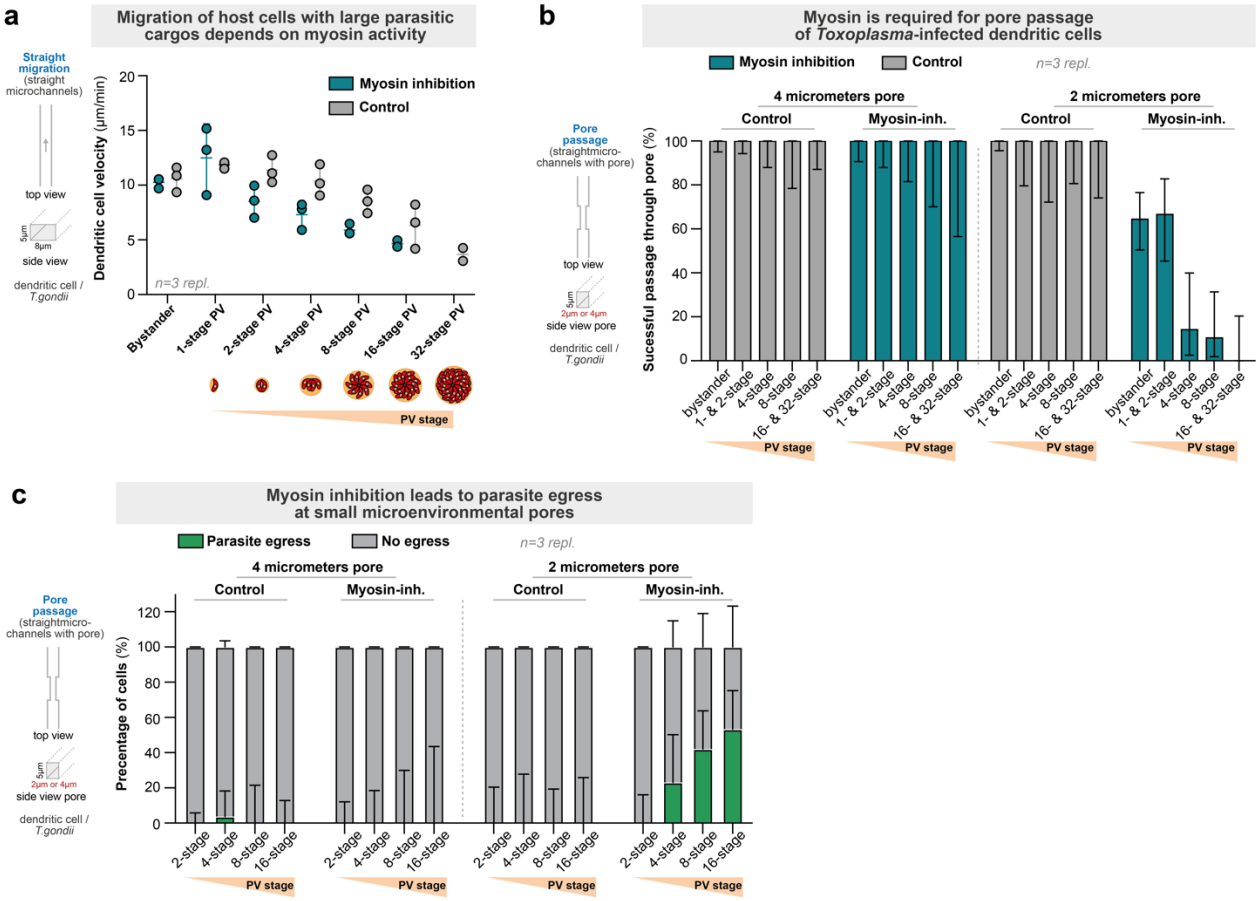

Figure 4. Intracellular parasitic repositioning and host cell contractility facilitate crossing of microenvironmental barriers. (A) Dendritic cell migration velocity through 8 micrometers-wide microchannels upon *Toxoplasma gondii* infection, in presence of the myosin II inhibitor para-nitro-blebbistatin or DMSO controls. N=3 individual biological replicates. **(B)** Dendritic cell migration passing time through 4 and 2 micrometers-wide microchannel pores upon *Toxoplasma gondii* infection, in presence of the myosin II inhibitor para-nitro-blebbistatin or DMSO controls. N=3 individual biological replicates. **(C)** Parasitic egress upon migration or attempt migration through 4 and 2 micrometers-wide microchannel pores upon *Toxoplasma gondii* infection, in presence of the myosin II inhibitor para-nitro-blebbistatin or DMSO controls. N=3 individual biological replicates

498 **Methods**

499 **Cell culture.**
500 Cells were maintained at 37°C in a humidified incubator with 5% CO_2 in basis medium of
501 RPMI-1640 medium (Invitrogen, 21875034) containing 10% fetal bovine serum (Gibco,
502 10437-028), 1% penicillin-streptomycin (Sigma-Aldrich, P0781, 100 U/ml penicillin and 100
503 µg/ml streptomycin), 50 µM 2-mercaptoethanol (Gibco, 31350-010). For the culture of
504 immortalized hematopoietic precursor cells (Hoxb8 cell[30]), the basis medium was
505 supplemented with 5% culture supernatant of Flt3l secreting cells and 1 µM estradiol (Sigma-
506 Aldrich, E2758-1G).
507
508 **Bone marrow isolation from mice**
509 All animal experiments were performed in accordance with the German Animal Welfare Act.
510 The Core Facility Animal Models of the Biomedical Center (BMC) at LMU Munich housed
511 the used mice. Bone marrow from male and female C57Bl6/J mice sacrificed at age 8 to 12
512 weeks was used for the generation of bone marrow-derived dendritic cells (BMDCs). For this,
513 mice were euthanized by cervical dislocation, femurs and tibiae were isolated, cut open and
514 flushed with basis medium.
515
516 **Differentiation of dendritic cells**
517 DCs were differentiated from Hoxb8 progenitor cells or murine bone marrow derived
518 progenitor cells. Progenitor cells were seeded in basis medium supplemented with 10% culture
519 supernatant of GM-CSF secreting cells. On day 3, 20% GM-CSF medium was added 1:1 to the
520 cells without pipetting the cells. On day 6, half the culture medium was replaced with 20%
521 GM-CSF medium without pipetting the remaining cells. On day 8 cells were frozen in fetal
522 bovine serum (FBS, Gibco, 10437-028) supplemented with 10% DMSO, first for 3 day at -70C
523 in a suitable Freezing Container then stored for up to 1 year in liquid Nitrogen storage. Cells
524 were used after fast thawing in 37 °C water bath and washing in basis medium, cells were
525 resuspended in basis medium supplemented 10 % GM-CSF medium, 1 million cells were
526 seeded in 3 ml medium per well of a 6 well plate.
527
528 **Culturing of *Toxoplasma gondii* parasites**
529 Toxoplasma cell line was tagged with HALO following standard protocols established in the
530 lab [31]. Parasites were maintained on HFFs (Human foreskin fibroblasts (HFFs) (RRID:
531 CVCL_3285, ATCC) in DMEM (Dulbecco's modified Eagle's medium), 10% fetal bovine
532 serum, 2 mM L-glutamine and 25 mg/ml gentamicin, and maintained at 37°C and 5% CO2.
533 Cultured cells and parasites were screened against mycoplasma contamination with LookOut
534 Mycoplasma detection kit (Sigma) and Mycoplasma Removal Agent (Bio-Rad) if needed.
535
536 **Infection of dendritic cells with *Toxoplasma gondii* parasites**
537 HFFs 4cm dish cell cultures were infected with $5x10^6$ parasites and left to replicate for 48h
538 until replicating vacuoles were ready to egress. Following the established protocols in the lab[32],
539 parasites were released by process of scratching and syringing, and then filtered to remove cell
540 debris. Next, toxoplasma cells were centrifuged at 300 g for 5 min and resuspended in
541 prewarmed PBS, washed again and resuspended in prewarmed basis media supplemented with
542 10% GM-CSF medium. DCs were infected by incubating $0.5x10^6$ parasites with $1x10^6$ DCs
543 for 20 h in 3 ml basis media supplemented with 10% GM-CSF medium in the well of a 6 well
544 plate. Cells were stained for 50 min with Janelia dye 646 HaloTag ligand (Promega, GA1120)
545 and Hoechst 33342, two drops of NucBlue (Invitrogen, R37605) per 3ml cells, pelleted at 300g
546 for 5 min and resuspended in basis medium with inhibitors or DMSO according to the

experimental requirements. For imaging, imaging medium was used, phenol-free basis medium supplemented with 50 µM L-ascorbic acid (MilliporeSigma, W210901) to limit photobleaching and phototoxicity.

PDMS microchannel assays:

Microchannels were generated as described previously described [33] Polydimethylsiloxane (PDMS, Sylgard 184, Biesterfield) was mixed, elastomer and curing agent 1:10, poured over silicon wafer with the negative microchannel structures imprinted by photolithography, degassed in vacuum, and cured at 80 °C overnight. The PDMS was cut to micro devices of approx. 7x12 mm in size, 2 holes of 2x7 mm were punched with 1 mm distance in between using a custom-made puncher, then the devices and glass coverslips that had been cleaned with isopropanol and ethanol were cleaned in a plasma cleaner and bonded at 120 °C. The PDMS devices were glued to a multi well plate. After 2 min plasma cleaner the microchannels were flooded with imaging medium, and equilibrated in the cell culture incubator. 0.625 µg/ml CCL19 were loaded into one hole and $50x10^3$ infected and stained dendritic cells in the other hole. Imaging was started as soon as the first cells entered into the microchannels.

Live cell imaging.

Live-cell imaging was performed using a Leica DMi8 inverted wide-field epifluorescence microscope with motorized stage and cell culture conditions of 37 °C and humidified 5 % CO2 (Pecon). Time-lapse recordings were performed using a 20x (Leica HC PL APO 20x/0.80, 11506529) or 40x (Leica HC PL APO 40x/0.95 CORR, 11506414) Lenses. The Leica sCMOS Camera DFC9000 GT was used as camera, LED5 fluorescence light source. Toxoplasma JF640 signal was imaged with a far-red filter (Excitation: 638/31, Emission: 695/58) and 640 nm excitation, EB3-mcherry with an orange filter (Excitation: 554/24, Emission: 594/32)) and 550 nm excitation, signal the nuclear Hoechst signal with a blue filter (Excitation: 391/32, Emission: 435/30) and 395 nm excitation. Exposure to 395 nm light was kept to a bare minimum, just enough to clearly localize the nucleus position and size, to avoid photo toxicity affecting experimental results.

Inhibitor experiments

Inhibitors were added to the imaging medium and added to the cells after staining, and the experimental environment, and CCL19 medium aswell. Para-Nitroblebbistatin was used at 25 µM with the same volume of DMSO as control, here a 1:2000 dilution. Nocodazol was used at 1 µM with the same volume of DMSO as control, here a 1:3333 dilution.

Image Analysis.

Fiji (version 2.14.0, [34] and LAS X (Version 3.7.6) were used for image processing. Only cells not interacting with other cells, and with single 1-32 stage PVs or uninfected bystanders were analyzed. For each cell individual parasite cells inside the PV were counted to assess the PV stage. All data was grouped accordingly. Cells positions were tracked using ROI manager of Fiji and quantified, exported, or merged to kymographs using custom made ImagJ scripts. Single cell data was analyzed with R (R version: 4.3.3, R-studio version 2023.12.1.402, tidyverse package version 2.0.0) and exported to GraphPad Prism (version 8.0.1) for statistical analysis.

Analysis of migration in straight channels: PV – host nucleus axis, migration speed, PV size

For orientation of *Toxoplasma* PV – host nucleus axis, cells were analyzed migrating in 8, 10 or 16 µm wide and 5 µm high PDMS channels. In imaging medium alone or supplemented with DMSO or inhibitors as indicated in the figure legends. Cells were imaged from ~100 to 600 µm after entering channels, PV-nucleus orientation, position, was documented at the beginning and end of the frame, from which orientation changes and average migration speed was calculated. PV or nucleus size was measured as the length of the PV or nucleus in direction of the channel, representing the major axis of the PV area. Cells were imaged at constant time interval that was

599 depending on the replicate between 45 and 75 seconds, except for the unfolding analysis, here cells
600 were recorded every 10 s.
601
602 **Analysis of migration in 2 and 4 µm constriction channels**
603 For each cell first time point of entering the channel of the cell, the nucleus, and the PV,
604 respectively, as well as first timepoint in which the cell, PV, and nucleus, respectively, fully exited
605 the constriction were documented. From the difference in time the passing time was calculated.
606 Further cells that did not exit the constriction during the recording of 5 h were documented to
607 calculate percentage of passed and stuck cells. Egress also was documented. Cells were imaged at
608 2 min time interval.
609
610 **Analysis of eb3-mcherry live fluorescence analysis.**
611 DCs derived from EB3-mcherry or Myosin-GFP expressing Hoxb8 cells were imaged while
612 migrating in 8 µm wide and 5 µm high microchannels. For the MTOC orientation analysis cells
613 with a clearly defined MTOC, as a single brightest spot in the EB3-mcherry fluorescence single
614 that was consistently present the recording time, were used. PV-Nuc-MTOC axis orientation was
615 documented after cells migrated roughly 300-500 µm in the channels.
616
617 **Analysis of myosin-GFP live fluorescence analysis.**
618 Myosin-GFP signal was analyzed first in 2 µm constriction channels. Kymographs of cells passing
619 2 µm constriction were generated. As the fluoresce localization did not notably change during pore
620 passage, the localization of Myosin-GFP analysis was analyzed in straight PDMS microchannels
621 of 8 µm width and 5 µm height. Myosin-GFP was categorized into predominantly in front,
622 predominantly in the rear, or diffuse signal, where fluorescence was not clearly localized neither to
623 the front or back but present everywhere.
624
625 **Statistics.** All experiments were performed at least as three independent biological replicates.
626 All replicates were validated independently. Statistical analysis was conducted using GraphPad
627 Prism (version 8.0.1) using the appropriate tests according to normal or non-normal data
628 distribution as stated in the figure legend. Fractional of cell subpopulations was calculated from
629 pooled cell numbers of at least three independent biological replicates, 95% confidence of the
630 fractions were calculated using the Wilson/Brown hybrid method. Error bars are defined in the
631 figure legends.
632
633

Acknowledgements

We thank Kasia Stefanowski for excellent technical assistance, Ana-Maria Lennon-Dumenil and Aline Yatim for bone marrow from MyoIIA-Flox*CD11c-Cre mice, Michael Sixt for Myh9-GFP expressing HoxB8 cells, and the Core Facility Bioimaging, the Core Facility Flow Cytometry, and the Animal Core Facility of the Biomedical Center (BMC) for excellent support. This study was supported by the Deutsche Forschungsgemeinschaft (DFG; German Research Foundation; Priority Programme SPP2332, project 492014049, to JR and BS; and DFG project ME 2675/6-2 to JP), the Peter Hans Hofschneider Professorship of the foundation "Stiftung Experimentelle Biomedizin" (to JR), the LMU Institutional Strategy LMU-Excellent within the framework of the German Excellence Initiative (to JR), and the European Research Council (ERC) under the European Union's Horizon 2020 research and innovation programme (BacForce, G.A.No. 852585, to BS).

Author contributions

Mauricio J.A. Ruiz-Fernandez: Conceptualization; investigation; methodology; writing - original draft; writing – review and editing.
Jianfei Jiang: Software and simulation; methodology; writing – review and editing.
Armina Mortazavi: investigation; methodology; writing – review and editing.
Bingzhi Wang: investigation; writing – review and editing.
Artur Kuznetcov: investigation; writing – review and editing.
Jack Merrin: Methodology; writing – review and editing.
Markus Meissner: Supervision; methodology; writing – review and editing.
Javier Periz: Conceptualization; supervision; investigation; writing – review and editing.
Benedikt Sabass: Conceptualization; supervision; investigation; funding acquisition; project administration; writing – review and editing.
Jörg Renkawitz: Conceptualization; supervision; investigation; funding acquisition; project administration; writing - original draft; writing – review and editing.

Competing interest declaration

The authors declare no competing interests.

Data availability

All data supporting the findings of this study are available within the paper. Requests for materials should be addressed to Jörg Renkawitz, Benedikt Sabass, and Javier Periz.

Additional information

Correspondence should be addressed to Jörg Renkawitz, Benedikt Sabass, and Javier Periz.